Interaction of a boundary layer with a turbulent wake

Ugo Piomelli
Department of Mechanical Engineering
University of Maryland
College Park, MD 20742

Final Report for Grant NAG12285
monitored by Dr. M. M. Choudhari

The objective of this grant was to study the transition mechanisms on a flat-plate boundary layer interacting with the wake of a bluff body. This is a simplified configuration, sketched in Fig. 1, designed to exemplify the phenomena that occur in multi-element airfoils, in which the wake of an upstream element impinges on a downstream one. Some experimental data is available for this configuration [1—3] at various Reynolds numbers.

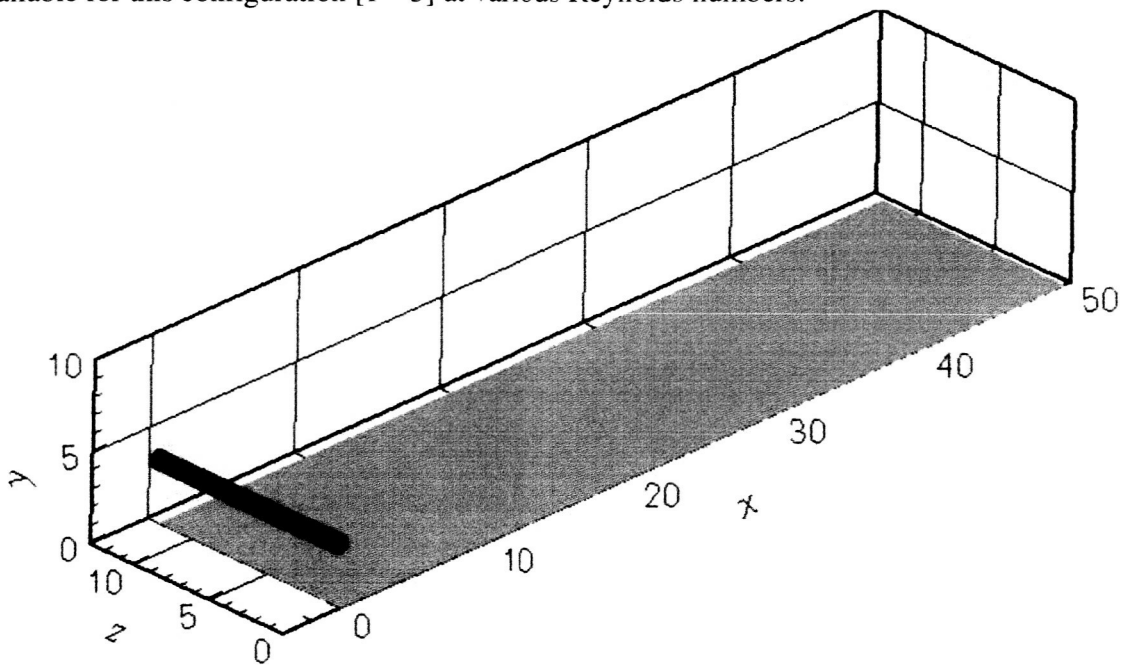

Figure 1 Sketch of the geometric configuration.

The first task carried out was the implementation and validation of the immersed-boundary method [4, 5]. This was achieved by performing calculations of the flow over a cylinder at low and moderate Reynolds numbers. The low-Reynolds number results are discussed in Ref. 6,

which is enclosed as Appendix A. The high-Reynolds number results are presented in a paper in preparation for the *Journal of Fluid Mexhanics.*

We performed calculations of the wake/boundary-layer interaction at two Reynolds numbers, Re=385 and 1155. The first case is discussed in Ref. 6, and a comparison of the two calculations is reported in Ref. 7. The simulations indicate that at the lower Reynolds number the boundary layer is buffeted by the unsteady Karman vortex street shed by the cylinder. This is shown in Fig. 2: long streaky structures appear in the boundary layer in correspondence of the three-dimensionalities in the rollers. The fluctuations, however, cannot be self-sustained due to the low Reynolds-number, and the flow does not reach a turbulent state within the computational domain. In contrast, in the higher Reynolds-number case, boundary-layer fluctuations persist after the wake has decayed (due, in part, to the higher values of the local Reynolds number Re achieved in this case); some evidence could be observed that a self-sustaining turbulence generation cycle was beginning to be established.

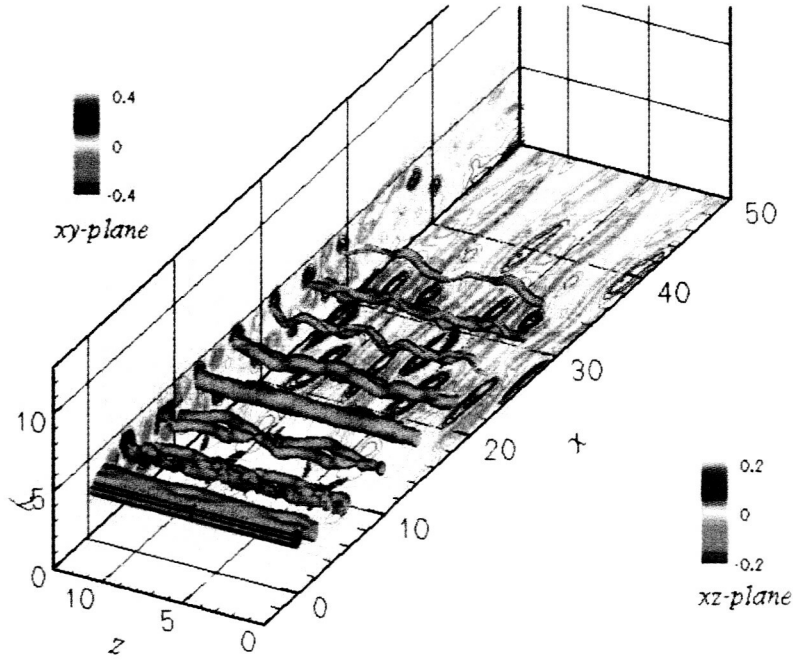

Figure 2 Instantaneous flow field for the Re=385 calculation. Iso-surfaces of pressure and streamwise velocity fluctuations.

A third simulation was subsequently carried out at a higher Reynolds number, *Re*=3900. This calculation gave results similar to those of the *Re*=1155 case. Turbulence was established at fairly low Reynolds number, as a consequence of the high level of the free-stream perturbation. Figure 3 shos an instantaneous flow visualization for that case.

A detailed examination of flow statistics in the transitional and turbulent regions, including the evolution of the turbulent kinetic energy (TKE) budget and frequency spectra showed the formation and evolution of "turbulent spots"' characteristic of the bypass transition mechanism. It was also observed that the turbulent eddies achieved an equilibrium, fully developed turbulent states first, as evidenced by the early agreement achieved by the terms in the TKE budget with those observed in turbulent flows (Figs. 4 and 5). Once a turbulent Reynolds stress profile had been established, the velocity profile began to resemble a turbulent one, first in the inner region and later in the outer region of the wall layer. An extensive comparison of the three cases, including budgets, mean velocity and Reynolds stress profiles and flow visualization, is in Ref. 8.

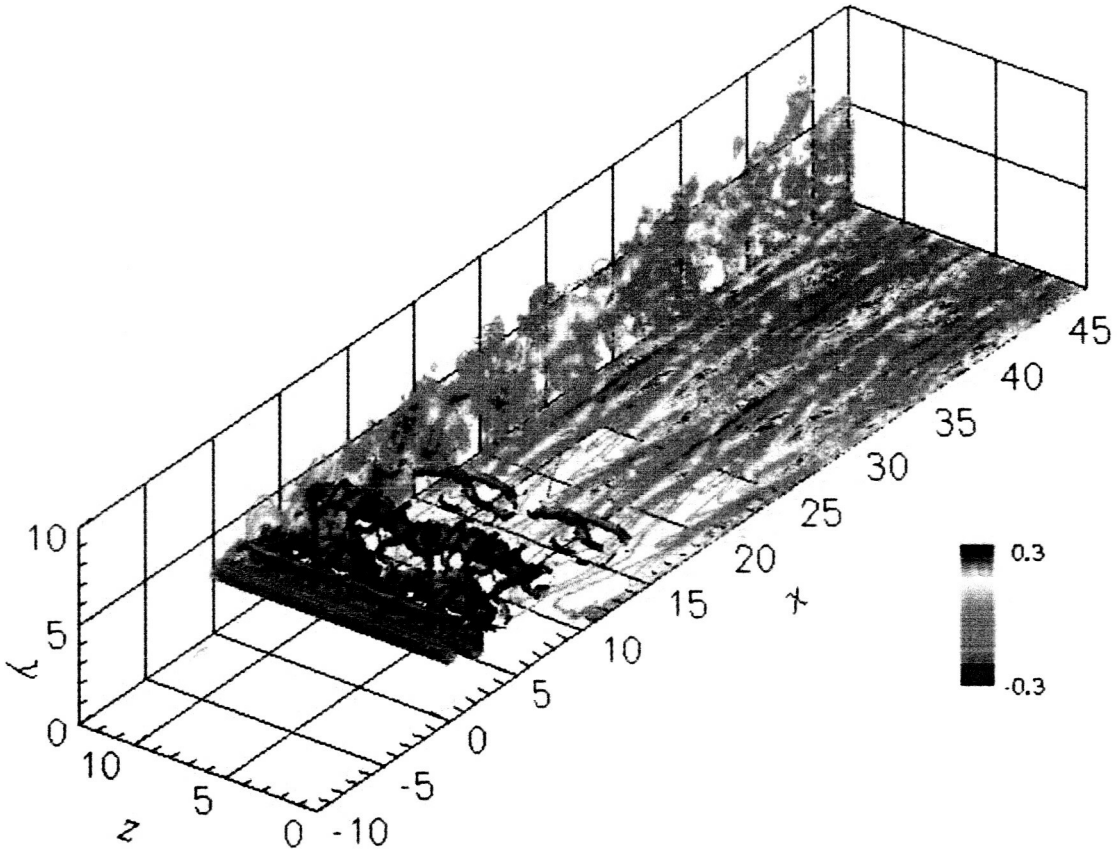

Figure 3 Instantaneous flow field for the Re=3900 calculation. Iso-surfaces of pressure and streamwise velocity fluctuations.

Copies of Refs. 6 and 7, which discuss the results obtrained, are enclosed.

References

Underlined articles acknowledge NASA support.

1. Kyriakides NK, Kastrinakis EG, Nychas SG, Goulas, A 1996. *Proc. Inst. Mech. Eng* **21**, 167.
2. Kyriakides NK, Kastrinakis EG, Nychas SG, Goulas, A 1999. *AIAA J.* **37**, 1197.
3. Kyriakides NK, Kastrinakis EG, Nychas SG, Goulas, A 1999. *Eur J. Mech. B-Fluid* **18**, 1049.
4. Fadlun EA, Verzicco R, Orlandi P, Mohd-Yusof J 2000. *J. Comput. Phys.* **161**, 35.
5. Verzicco R, Mohd-Yusof J, Orlandi P, Haworth, D 2000. *AIAA J.* **38**, 427.

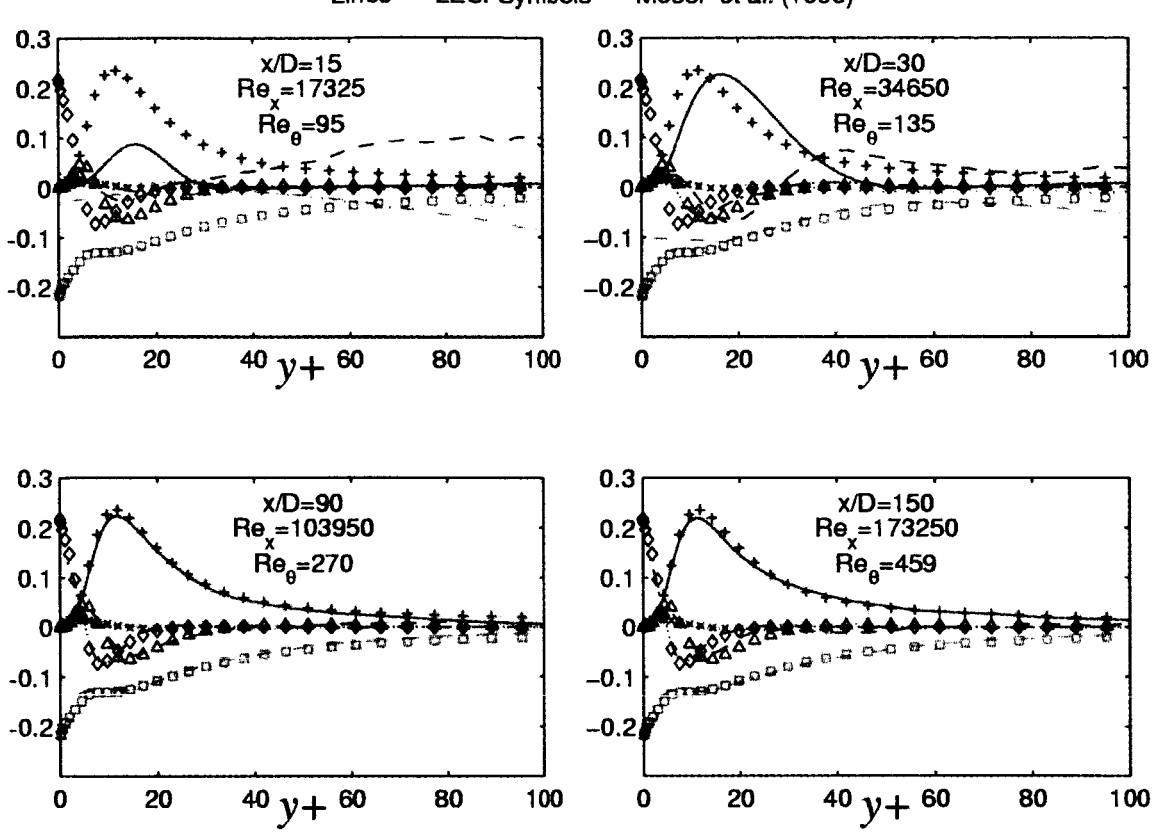

Figure 4 Turbulent kinetic energy budgets, Re=1155.

6. Piomelli U, Balaras E 2001 In *DNS/LES Progress and Challenges*, eds. C. Liu, L. Sakell and T. Beutner, (Greyden Press, Columbus), pp. 105—116.
7. Piomelli U, Choudhari MM, Ovchinnikov V, Balaras E 2003 *AIAA Paper 2003-0975.*
8. Ovchinnikov V, Piomelli U, Choudhari MM 2004 To be submitted to *J. Fluid Mech.*

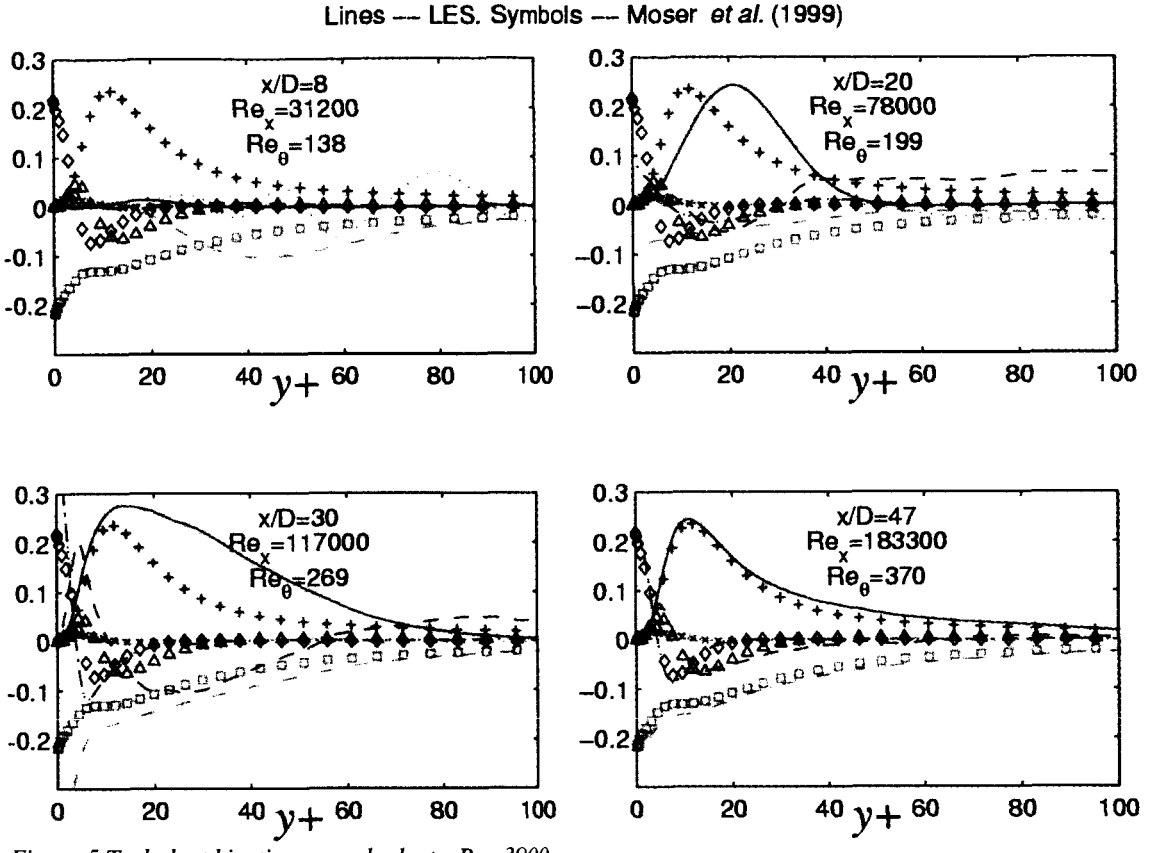

Figure 5 Turbulent kinetic energy budgets, Re=3900.

NUMERICAL SIMULATIONS USING THE IMMERSED BOUNDARY TECHNIQUE

UGO PIOMELLI AND ELIAS BALARAS
Department of Mechanical Engineering
University of Maryland
College Park, MD 20742 - USA

Abstract. The immersed-boundary method can be used to simulate flows around complex geometries within a Cartesian grid. This method has been used quite extensively in low Reynolds-number flows, and is now being applied to turbulent flows more frequently. The technique will be discussed, and three applications of the method will be presented, with increasing complexity, to illustrate the potential and limitations of the method, and some of the directions for future work.

1. Introduction

The increase in computer speed achieved over the last few years has made computational fluid dynamics increasingly useful and widespread as a tool to analyze and design flow configuration. Complex geometries, however, present an obstacle even to present-day computers, since the use of body-fitted meshes (structured or unstructured) significantly increases the cost of a calculation in terms of both computational speed and memory requirements.

An alternative method that may be cost-efficient in many situations is the "immersed-boundary" method. This technique is based on the introduction of body forces distributed throughout the flow that mimic the effect that a solid body would have on the fluid. This approach allows the use of codes in Cartesian coordinates, which present significant advantages, in terms of speed, accuracy and flexibility, over codes that employ body fitted grids.

This idea has been widely used in hæmo-dynamics and bio-fluids engineering: two- and three-dimensional calculations of the flow in the heart

were reported by Peskin [13, 14] and McQueen and Peskin [8, 9]. In these calculations the motion of the boundary was determined by the fluid itself, so that the boundary had to be modeled as a set of elements linked by springs. In cases in which the boundary motion is known *a priori*, the problem can be significantly simplified.

Goldstein *et al.* [4] proposed a feedback forcing mechanism that forces the fluid velocity u_i to approach the velocity of the solid boundary, V_j, on the boundary itself. Consider the incompressible Navier-Stokes equations:

$$\frac{\partial u_j}{\partial x_j} = 0, \tag{1}$$

$$\frac{\partial u_i}{\partial t} + \frac{\partial}{\partial x_j}(u_j u_i) = -\frac{1}{\rho}\frac{\partial p}{\partial x_i} + \nu \nabla^2 u_i + f_i. \tag{2}$$

Goldstein *et al.* [4] assigned a force field

$$f_i(x_{s,i}, t) = \alpha_f \int_0^t [u_i(x_{s,i}, t) - V_i(x_{s,i}, t)]\, dt' + \beta_f [u_i(x_{s,i}, t) - V_i(x_{s,i}, t)], \tag{3}$$

where α_f and β_f are two negative constants, and $x_{s,i}$ are the coordinates of the solid surface. The net effect of this force is to tend to annihilate the velocity difference $u_i - V_i$. The flow, in fact, responds to the forcing as a damped oscillator (see [4] and [3] for an in-depth discussion of this issue); the frequency of the oscillator is $\propto |\alpha_f|^{1/2}$, whereas its damping coefficient is $\propto \beta_f/|\alpha|^{1/2}$. This implies that, in order to enforce the no-slip condition effectively, α_f and β_f must have large magnitudes (larger than the highest frequency in the flow), which make the equations stiff. If the forcing is advanced in time explicitly, in fact, the maximum allowable CFL is $o(10^{-3})$; even implicit methods only allow the use of CFL numbers of 0.1 or less. This constraint makes this method impractical for the calculation of unsteady (in particular, turbulent) flows.

Recently, Mohd-Yusof [11] proposed the "direct forcing method," which assigns a force field given by

$$f_i = \frac{\partial}{\partial x_j}(u_j u_i) + \frac{1}{\rho}\frac{\partial p}{\partial x_i} - \nu \nabla^2 u_i + \frac{V_i - u_i}{\Delta t}, \tag{4}$$

(where the dependence on $x_{s,i}$ and t has been omitted). This forcing imposes directly the desired velocity on the immersed boundary, and has the advantage (over the feedback forcing method) that it does not require significant reductions in the allowable time-step. It was extensively tested in a staggered finite-difference code by Fadlun *et al.* [3], who derived an interpolation scheme to be used when the boundary does not coincide with a grid

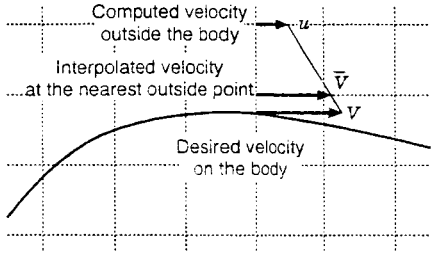

Figure 1. Interpolation method used to apply the forcing.

line. Verzicco *et al.* [15] applied this method to the large-eddy simulation of high Reynolds number turbulent flows by calculating the flow inside an IC engine.

In the present paper additional applications of this method will be presented, and the potential and limitations of the technique, as well as issues that require further study, will be discussed. After a brief review of the governing equations and of the numerical scheme used, three test cases will be shown: a low Reynolds-number flow over a cylinder in the presence of a moving surface (Wannier [16] flow), the flow over a circular cylinder at low Reynolds number, and the bypass transition on a flat plate caused by the interaction between the boundary layer and the wake of a circular cylinder.

2. Problem formulation

Governing the flow are the incompressible Navier-Stokes equations (1-2). The flow solver is a standard 2nd-order accurate method on a staggered mesh [1]. The fractional time-step method [2, 6] is used and a 2nd-order accurate Adams-Bashforth method is employed for the time advancement. A non-reflecting boundary condition [12] is used at the outflow, and periodic boundary conditions in the spanwise direction. The inflow and free-stream conditions depended on the case studied.

The direct forcing (4) was used. Since the immersed body does not follow a grid line the interpolation method proposed by Fadlun *et al.* [3] is used. The forcing is imposed not at the surface itself, but at the first point outside it (see Fig. 1) and the solid body velocity in (4) is replaced with the velocity $\overline{V_i}$ obtained by a linear interpolation between the computed fluid velocity outside the body, u_i, and the desired body velocity V_i. This method has several advantages: first, it has been shown to be fully second-order accurate in time [3]; therefore, it is consistent with the second-order differencing scheme used by the solver; secondly, since it assumes that the velocity profile is linear near the body, it implies homogeneous Neumann

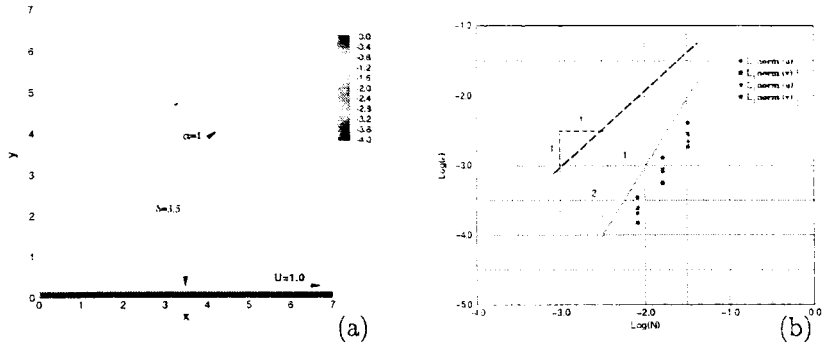

Figure 2. Wannier flow test case (Wannier 1950). (a) Computational domain and computed streamlines; (b) L_1 and L_2 norms of the error, ϵ, for u and v velocity components. N is the total number of grid points.

boundary conditions for the pressure (see the Appendix in [3] for a full discussion of this issue). This last feature is very important in the framework of fractional time-step methods, since it implies that the corrector step does not result in a modification of the body velocity imposed through the forcing in the Helmholtz step. On the other hand, the assumption that the velocity profile is linear over the first two layers of cells outside the immersed body requires the use of a very fine mesh in the vicinity of the body.

3. Results and discussion

3.1. WANNIER FLOW

A straightforward way to verify the accuracy of the proposed methodology is to compute a flow containing a curved immersed boundary for which an analytical solution exists. The case considered here is the Stokes flow around a cylinder in the vicinity of a moving wall (see Fig. 2). An analytical solution for this case was derived by Wannier [16]. The streamlines for this flow are shown in Fig. 2a. Three computations on gradually finer uniform grids (32×32, 64×64, and 128×128) were conducted. The L_1 and L_2 norms of the error (the difference between the computed and analytical solution) are shown in Fig. 2b as a function of the total number of points N. The error decreases with a -2 slope indicating that the proposed methodology is second order accurate.

3.2. FLOW OVER A CIRCULAR CYLINDER

The next test case examined is the flow over a circular cylinder at $Re_D = U_\infty D/\nu = 300$ (where D is the cylinder diameter and U_∞ the free-stream

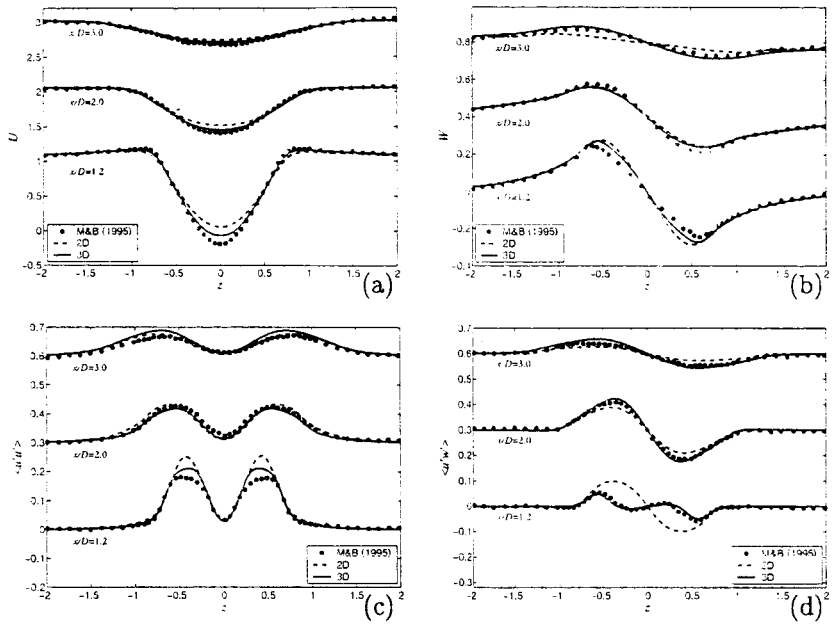

Figure 3. Flow over a circular cylinder, $Re_D = 300$. Velocity statistics. (a) U, (b) W, (c) $\langle u'u' \rangle$, (d) $\langle u'w' \rangle$. Reference data from Ref. [10].

velocity). Two calculations will be compared: a 2D one that used 400×200 points in the $xz-$plane, and a 3D one, with the same mesh in the $xz-$plane, and 48 points in y. The computational domain was $60 \times 2\pi \times 30$, and the cylinder center was at $x_c = 10$, $z_c = 15$ (all lengths are made dimensionless by D, all velocities by U_∞). The grid was stretched both in the $x-$ and $z-$directions; the last 1/6 of the domain (which required only 10 grid points in x) formed a sponge region, used to minimize the upstream propagation of disturbances due to the convective outflow conditions. A uniform velocity profile was imposed at the inlet, and slip-wall conditions were applied at $z = 0$ and $z = 30$.

The velocity statistics are shown in Fig. 3. Here and in the following the angle brackets denote averaging in time and in the spanwise direction. The 3D calculation is in very good agreement with the reference data by Mittal and Balachandar [10]. At this Reynolds number, three-dimensionality is observed in the wake, which is evidenced in the visualization in Fig. 4, which shows iso-surfaces of the second invariant of the velocity-gradient tensor,

$$Q = -\frac{1}{2}\frac{\partial u_i}{\partial x_j}\frac{\partial u_j}{\partial x_i} = -\frac{1}{2}\left(S_{ij}S_{ij} - \Omega_{ij}\Omega_{ij}\right), \tag{5}$$

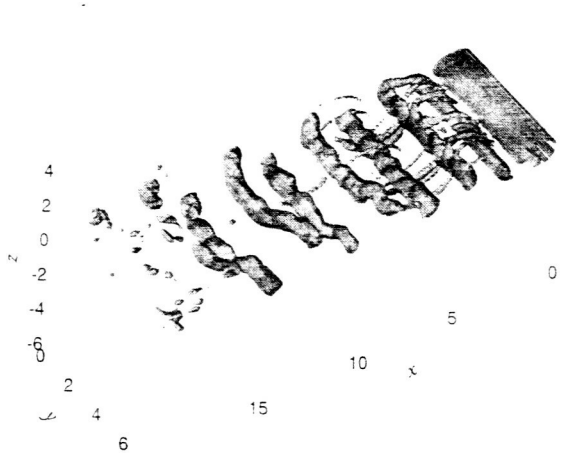

Figure 4. Flow over a circular cylinder, $Re_D = 300$. Isosurfaces of $Q = 0.6$.

(where $\overline{\Omega}_{ij}$ is the anti-symmetric part of the velocity gradient tensor). The condition $Q > 0$ identifies effectively the regions of coherent vorticity [5].

Figure 4 shows the formation of an instability on the initially 2D rollers, and the presence of quasi-streamwise rib vortices joining the rollers. The magnitude of the spanwise Reynolds stresses $\langle v'v' \rangle$, in this calculation, however, remained significantly smaller than the other two normal components, which allowed the 2D calculation to give reasonable results.

The effects of the grid resolution near the obstacle are shown in Fig. 5. The cell Reynolds number is defined as

$$Re_c = \frac{(\Delta x^2 + \Delta z^2)\,(u^2 + w^2)}{\nu}, \tag{6}$$

where u and w are the instantaneous velocities, and Δx and Δz the grid spacings. If the mesh is insufficiently fine ($Re_c > 30$), some oscillations can be observed that initiate along lines at $\pm 45^o$ on the cylinder (they are especially visible in the w contours, Fig. 5b). Refining the grid, thus reducing Re_c reduces the size of this oscillation (Figs. 7a and b). Two-dimensional interpolation schemes that use both the points indicated by the diamonds and those indicated by squares in Fig. 6 to determine $\overline{V}_i$ have also been found (Verzicco, private communication, 2001) to reduce the amplitude of these oscillations.

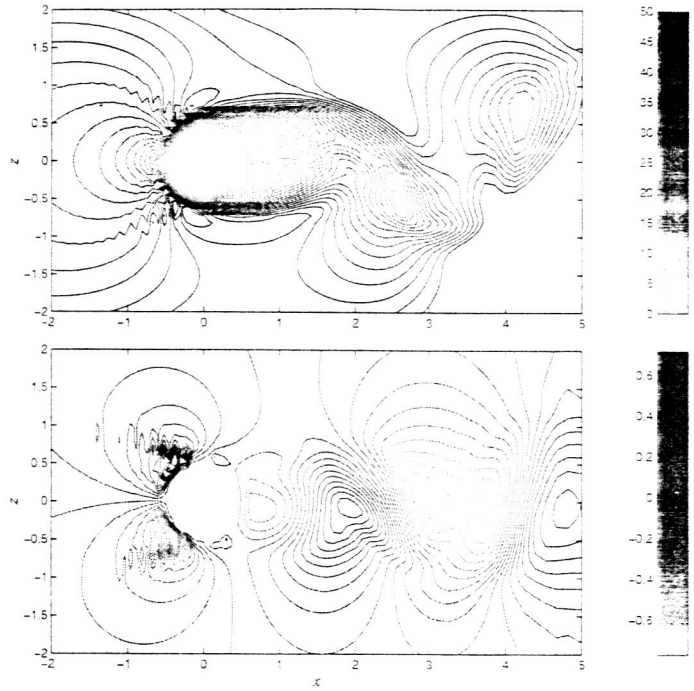

Figure 5. Flow over a circular cylinder, $Re_D = 300$. Coarse (200×100) 2D calculation. (a) Contours of the cell Reynolds number; (b) contours of w.

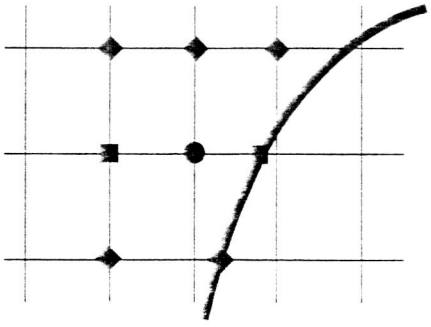

Figure 6. One-dimensional *vs.* two-dimensional interpolation stencils.

3.3. WAKE/BOUNDARY-LAYER INTERACTION

Wakes interact with laminar boundary layers in many applications of engineering interest, for example on the leading edge of multi-component

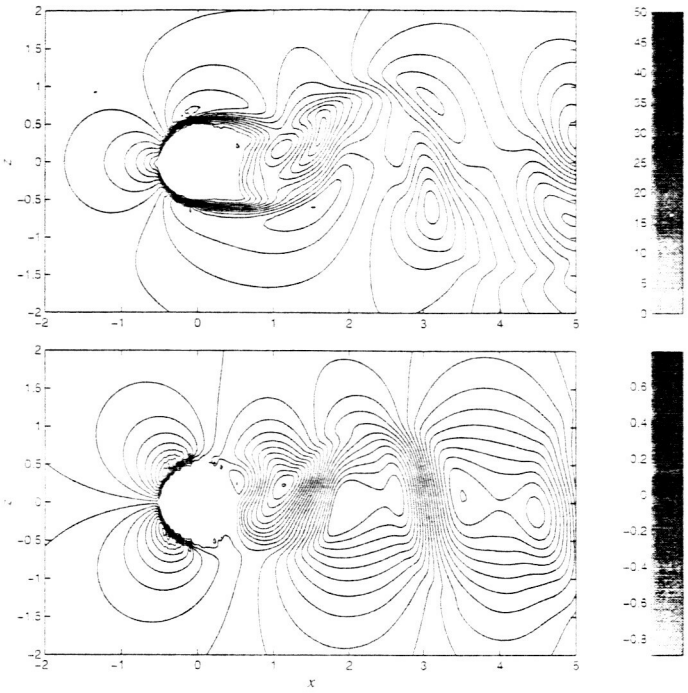

Figure 7. Flow over a circular cylinder, $Re_D = 300$. Fine (400 × 200) 2D calculation. (a) Contours of the cell Reynolds number; (b) contours of w.

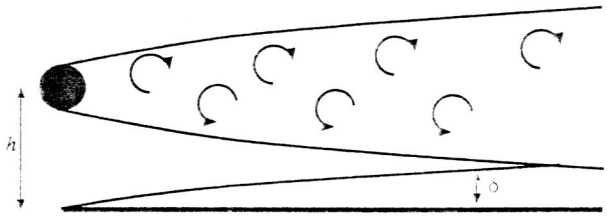

Figure 8. Sketch of the wake/boundary-layer configuration.

airfoils, or inside turbo-machinery. The interaction of the turbulent eddies present in the wake with the boundary layer itself then becomes a primary driver of the transition process in the boundary layer itself, and may lead to transition to turbulence at fairly low Reynolds numbers.

The configuration examined in the present study is sketched in Fig. 8. A circular cylinder, with its axis normal to the stream is placed above a

flat plate. The cylinder center is at $x_c = 10$, $z_c = 3.2$, immediately above the leading-edge of the plate, which was also at $x_c = 10$. As in the previous case, distances are normalized by D, velocities by U_∞. The computational domain was $60 \times 2\pi \times 20$. As for the cylinder calculation, the grid was stretched both in the $x-$ and $z-$directions and a sponge region was used. The Reynolds number based on cylinder diameter was 385. The configuration corresponds to Case 1 in the experimental paper by Kyriakides *et al.* [7], who observed significant velocity fluctuations in the boundary layer, starting from a point approximately six diameters downstream of the cylinder. These fluctuations are generated by the large-scale convective motion of the vortices, and do not die down after the wake has weakened, but develop into a turbulent boundary layer despite the fact that the Reynolds number is very low.

The distribution of the streamwise Reynolds stress, $\langle u'u' \rangle$, as a function of x is shown in Fig. 9. A sudden increase of $\langle u'u' \rangle$ can be observed to begin at $x = 8$, indicating the beginning of transition. This result is consistent with the observations of Kyriakides *et al.* [7], who defined the onset of transition as "the $x-$location where the velocity signal at the same height above the plate loses its sinusoidal character", and found that transition occurs at $x = 7.4$.

The velocity profiles, shown in Fig. 10a at several locations, initially resemble a Blasius profile merging into a wake near the cylinder. As the wake widens and interacts with the boundary layer, a logarithmic layer begins to establish itself, indicative of transition towards turbulent flow. This transitional behavior is also observed in the trace of the Reynolds stress tensor, q^2 (equal to twice the turbulent kinetic energy), which in the latter sections establishes a turbulent-like distribution, with a peak of magnitude $7 - 8\tau_w$ at $z^+ \simeq 10 - 12$. It should be noted that this quasi-turbulent state is achieved at very low Reynolds number: the boundary-

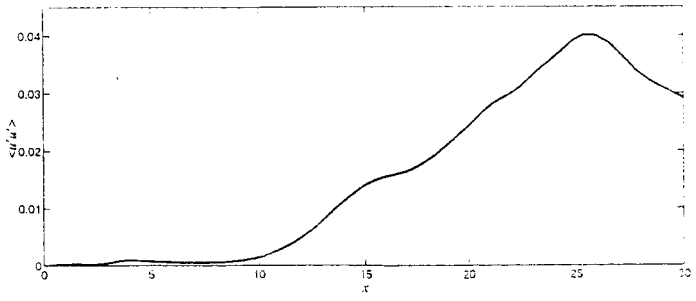

Figure 9. Wake/boundary-layer interaction. $\langle u'u' \rangle$ distribution at $z = 0.18$.

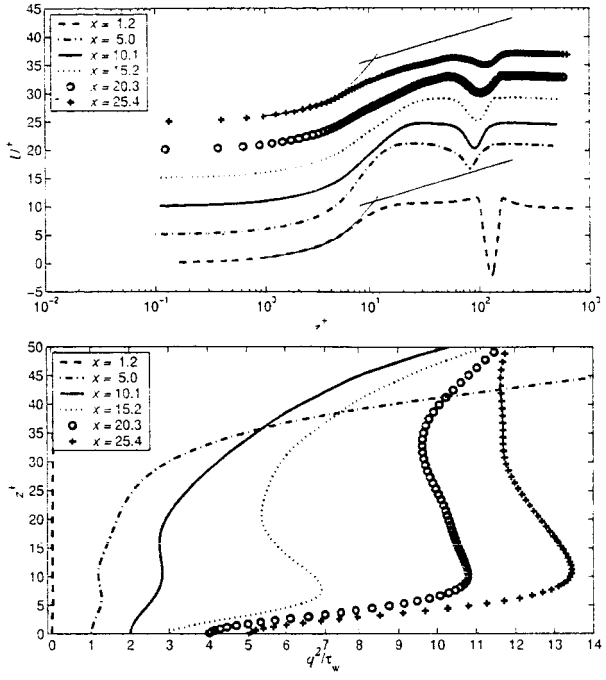

Figure 10. Wake/boundary-layer interaction. Turbulent statistics. Top: mean velocity profile; bottom: $q^2 = \langle u_i' u_i' \rangle$.

layer thickness δ (defined as the distance above the plate at which the first maximum of the velocity profile occurs) is approximately 50-70 wall units.

A visualization of the flow is shown in Fig. 11. The structure of the cylinder wake is similar to that highlighted in Fig. 4, with strong spanwise rollers that exhibit 3D instabilities and eventually break up, and smaller quasi-streamwise vortices in the braid region. The contours of streamwise velocity fluctuation u' on a plane parallel to the wall show significant levels of fluctuations, especially near kinks in the rollers belonging to the lower row. Quasi-streamwise streaks are formed around $x = 15$, whose spacing is approximately 100 wall units.

4. Conclusions

The immersed-boundary technique has been presented and discussed. Illustrative results from three simulations indicate the potential of this technique, which allows the calculation of flows around complex geometries without requiring a body-fitted grid.

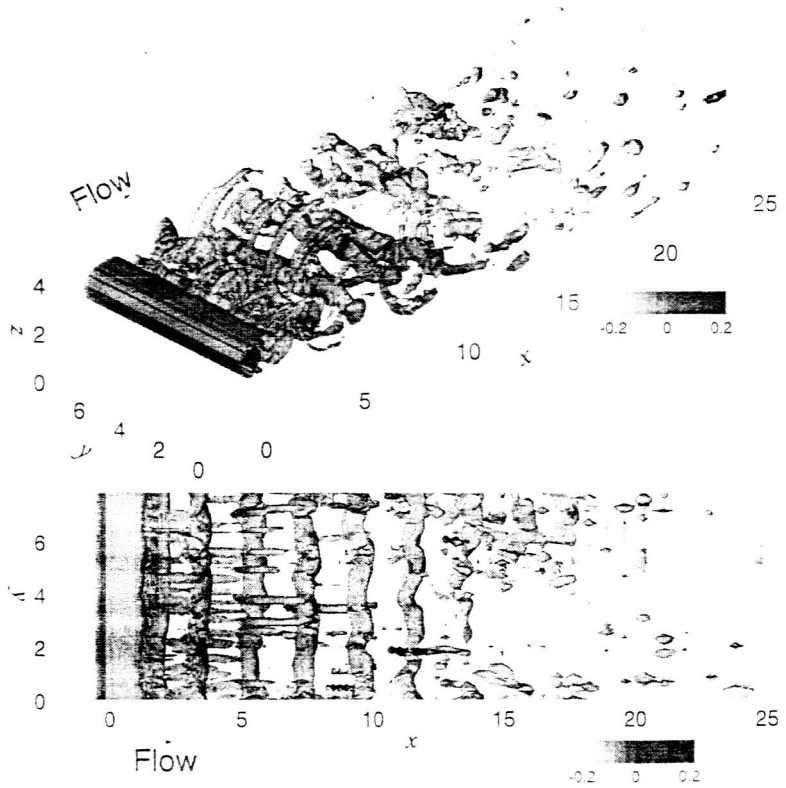

Figure 11. Wake/boundary-layer interaction. Isosurfaces of $Q = 0.4$ and contours of u' in the $z = 0.18$ plane. Top: perspective view; bottom: view from above.

If appropriate interpolation methods are used when the body does not coincide with a grid line, the method is second-order accurate. However, some care must be taken in the discretization of the flow field, especially in the vicinity of the body. We have observed the development of numerical oscillations when the cell Reynolds-number exceeded values of approximately 30. These oscillations did not grow or change position in time, and their effect on the flow field downstream of the obstacle was limited in the cases studied. This was observed, for instance, in calculations of the flow around the cylinder at $Re_D = 3500$ were carried out in which the grid could not be sufficiently refined to satisfy the cell-Reynolds-number requirement. However, it is not known whether these oscillations might give rise to instabilities in other geometries, or at higher Reynolds numbers. The development of more accurate, multi-dimensional interpolation schemes might be bene-

ficial in this respect. The use of multi-block methods, or embedded grids, could also alleviate this problem.

If these numerical schemes can be overcome, the immersed boundary method appears to be a useful tool for the simulation of flows in complex geometries at moderate or high Reynolds numbers. This is confirmed by the increasing number of studies using this method that are appearing in the literature.

Acknowledgments

Research supported by the NASA Langley research Center under Grant NAG12285 monitored by Drs. Craig L. Streett and Meelan M. Choudhari.

References

1. Balaras, E. 1995 *Ph. D. Thesis*, EPFL (Federal Institute of Technology–Lausanne, Switzerland).
2. Chorin, A.J. 1968 *Math. Comput.* **22**, 745.
3. Fadlun, E.A., Verzicco, R., Orlandi, P., Mohd-Yusof, J. 2000 *J. Comput. Phys.* **161** 35.
4. Goldstein, D., Handler. R. Sirovich, L. 1993 *J. Comput. Phys.* **105**, 354–366.
5. Hunt, J.C.R., Wray, A.A. and Moin, P. 1988 In *Center for Turbulence Research, Proc. Summer Program 1988*, 193.
6. Kim, J. and Moin, P. 1985 *J. Comput. Phys.* **59** 308.
7. Kyriakides N.K., Kastrinakis, E.G., Nychas, S.G., Goulas, A. 1996 *Proc. Inst. Mech. Eng.* **210**, 167.
8. McQueen, D.M., Peskin, C.S. 1989 *J. Comput. Phys.* **82** 289.
9. McQueen D.M., Peskin, C.S. 1997 *J. Supercomput.* **11** 213.
10. Mittal, R. and Balachandar, S. 1995 *Phys. Fluids* **7**, 1841.
11. Mohd-Yusof, J. 1997 in *CTR Annu. Res. Briefs 1997*, NASA Ames/Stanford University, 317.
12. Orlanski, I. 1976 *J. Comput. Phys.* **21**, 251.
13. Peskin, C.S. 1972 *J. Comput. Phys.* **10** 252.
14. Peskin, C.S. 1977 *J. Comput. Phys.* **25** 220.
15. Verzicco, R., Mohd-Yusof, J., Orlandi, P., Haworth, D. 2000 *AIAA J.* **38** 427.
16. Wannier, G. H. 1950 *Quart. Applied Mathematics* **8** 1.

AIAA 2003-0975

Numerical simulations of wake/boundary layer interactions

Ugo Piomelli
Department of Mechanical Engineering
University of Maryland, College Park, MD 20742

Meelan M. Choudhari
NASA Langley Research Center, Hampton, VA 23681

Victor Ovchinnikov and Elias Balaras
Department of Mechanical Engineering
University of Maryland, College Park, MD 20742

41st Aerospace Sciences
Meeting and Exhibit
6–9 January 2003
Reno, Nevada

Numerical simulations of wake/boundary layer interactions

Ugo Piomelli *
Department of Mechanical Engineering
University of Maryland, College Park, MD 20742

Meelan M. Choudhari †
NASA Langley Research Center, Hampton, VA 23681

Victor Ovchinnikov ‡and Elias Balaras §
Department of Mechanical Engineering
University of Maryland, College Park, MD 20742

Direct and large-eddy simulations of the interaction between the wake of a circular cylinder and a flat-plate boundary layer are conducted. Two Reynolds numbers are examined. The simulations indicate that at the lower Reynolds number the boundary layer is buffeted by the unsteady Kármán vortex street shed by the cylinder. The fluctuations, however, cannot be self-sustained due to the low Reynolds-number, and the flow does not reach a turbulent state within the computational domain. In contrast, in the higher Reynolds-number case, boundary-layer fluctuations persist after the wake has decayed (due, in part, to the higher values of the local Reynolds number Re_θ achieved in this case); some evidence could be observed that a self-sustaining turbulence generation cycle was beginning to be established.

Introduction

High-lift systems have a significant impact on the overall cost and safety of aircraft. According to Meredith,[1] a 1% improvement in the maximum lift coefficient (or lift-to-drag ratio) could translate into an increased payload of 14 to 22 passengers on a large twin-engine transport. An optimal aerodynamic design of a multi-airfoil high-lift configuration requires careful consideration of both inviscid and viscous flow phenomena. In particular, laminar-to-turbulent transition is a crucial issue for ground-to-flight scaling of high-lift flow fields.

Either of the familiar transition mechanisms for a single-element configuration are also relevant to transition over a multi-airfoil configuration: those associated with streamwise instabilities in the form of Tollmien-Schlichting or Rayleigh modes, cross-flow and attachment line instabilities, and leading-edge contamination—a form of subcritical (*i.e.*, bypass) transition. However, a unique transition mechanism in the case of multi-element flow-fields involves the boundary-layer contamination due to unsteady wake(s) from the preceding element(s) and/or additional forms of vortical disturbances originating from the separated, cove flow underneath an upstream element (Fig. 1). While the "single-element" class of transition mechanisms have been widely studied in the literature, the wake-contamination issue has received little scrutiny thus far and is the focus of this paper.

Interactions between turbulent wakes and boundary layers have been the subject of much study. Most of the investigations, however, concentrated on the unsteady case that occurs, for instance, in turbomachinery, when the wake of an upstream blade impinges on a downstream blade; the unsteadiness of the impingement region plays an important role in the dynamics of the flow. Fewer studies can be found of the steady case. Squire[2] summarizes much of the investigations conducted prior to 1989. Particularly important is the work by Zhou and Squire[3] who examined the interaction between the wake of an airfoil and a flat plate. They found that, a region in which the wake and boundary layer are separated by a potential core is followed by a merging zone, in which the velocity profile in the outer layer is substantially different from that in a regular flat-plate boundary layer. They also observed that the position of zero Reynolds shear stress

Fig. 1 Sketch of the wake/boundary-layer interactions on an airfoil.

*Professor, AIAA Senior Member
†Senior Research Scientist
‡Graduate Research Assistant
§Assistant Professor

and that of zero mean-velocity gradient do not coincide, an important issue for eddy-viscosity turbulent models.

Recently, Kyriakides and co-workers[4–6] performed a series of experiments involving the interaction between the wake of a large-aspect-ratio circular cylinder and a flat-plate boundary layer. These experiments spanned a range of Reynolds numbers and cylinder diameters, including cases in which the wake still contained coherent eddies in the interaction region (i.e., the so called case of "strong interaction") and others in which the interaction took place sufficiently far downstream of the cylinder, such that the spanwise rollers had decayed significantly (i.e., "weak interaction" cases). While they provided measurements for a range of Reynolds numbers, Kyriakides *et al.*[4–6] did not clarify how transition could occur (and turbulence could be self-sustained) at the lowest Reynolds numbers examined.

Due to the tremendous challenges inherent in a high-fidelity simulation of the wake-contamination problem, we also choose to study a simple, building-block problem, namely that of interaction between a flat-plate boundary layer and the wake of a circular cylinder that is placed above the flat plate. This model problem provides a reasonable balance between simplicity (two-dimensional geometry involving a combination of two canonical flow fields) and the numerical challenges of a complex-geometry simulation including the wake generator and a boundary layer. Simultaneously, it allows one to investigate a range of issues, such as the effect of Reynolds number and the role of the spacing between the cylinder and plate (which allows one to traverse the continuous range from strong wake interactions to weak interactions that are analogous to conventional free-stream turbulence). Effects of flow three-dimensionality and/or transverse pressure gradients (which lead to curved wakes) may also be captured, if necessary, by modifying the free-stream boundary conditions. Most significantly, a limited amount of experimental data is available for a range of flow and geometry parameters.[4–6]

In the present paper we report the initial results from a series of numerical experiments designed to study the physical phenomena underlying wake/boundary-layer interactions of this type. The first stage of this investigation involves the study of the strong interaction case, with the specific aims to clarify some issues left unresolved by the experimental studies, and to document the flow field in detail. In particular, we will focus on the issue of transition mechanisms at low Reynolds number, which was only partially addressed in the experiment. Thus, we choose to examine low Reynolds-number cases first, before attempting the more challenging simulations at higher Reynolds numbers. Future work will focus on the weak interaction case, as well as other shapes of wake generators.

Herein, we analyze direct and large-eddy simulations of two cases studied by Kyriakides *et al.*,[4] having the same geometry but different Reynolds numbers, which lead to different responses of the boundary layer to the unsteady wake in the free stream. Despite the simplicity of the geometrical configuration, conducting DNS and LES of the above problem is a challenge for most numerical methods available today. In the present study we model the effect of the cylinder using an "immersed boundary" formulation.[11] This approach enables one to use codes in Cartesian coordinates, which present significant advantages, in terms of speed, accuracy and flexibility, over codes that employ body-fitted grids.

The outline of the paper is as follows: the numerical formulation of the problem including the geometry of the cylinder-plate configuration are described first. Then, the numerical methodology will be presented. We will then present validation of the numerical tool in the context of two building-block problems relevant to the flow configuration of interest; results of the simulations will be compared with numerical and experimental data. Results for the wake/boundary-layer interaction are discussed next. Finally, conclusions and recommendations for future work are presented.

Problem formulation

In this work we present both DNS and LES results. In the DNS case, the Navier-Stokes equations are solved:

$$\frac{\partial u_j}{\partial x_j} = 0, \tag{1}$$

$$\frac{\partial u_i}{\partial t} + \frac{\partial}{\partial x_j}(u_j u_i) = -\frac{1}{\rho}\frac{\partial p}{\partial x_i} + \nu \nabla^2 u_i + f_i. \tag{2}$$

For the LES, we use the filtered equations of conservation of mass and momentum

$$\frac{\partial \overline{u}_j}{\partial x_j} = 0, \tag{3}$$

$$\frac{\partial \overline{u}_i}{\partial t} + \frac{\partial}{\partial x_j}(\overline{u}_j \overline{u}_i) = -\frac{\partial \overline{p}}{\partial x_i} + \frac{1}{Re_\tau}\nabla^2 \overline{u}_i - \frac{\partial \tau_{ji}}{\partial x_j} + \overline{f}_i \tag{4}$$

(where the over-bar denotes filtered variables and the effect of the subgrid scales appears through the SGS stresses $\tau_{ij} = \overline{u_i u_j} - \overline{u}_i \overline{u}_j$); f_i and $\overline{f}_i$ are the body forces used in the immersed-boundary method to enforce the no-slip conditions on the body.

For both DNS and LES, the equations of motion are solved numerically using a second-order accurate finite-difference method on a staggered grid. In all cases the grid is uniform in the spanwise direction y, stretched in the streamwise and normal ones (x and z, respectively) to allow accurate resolution of

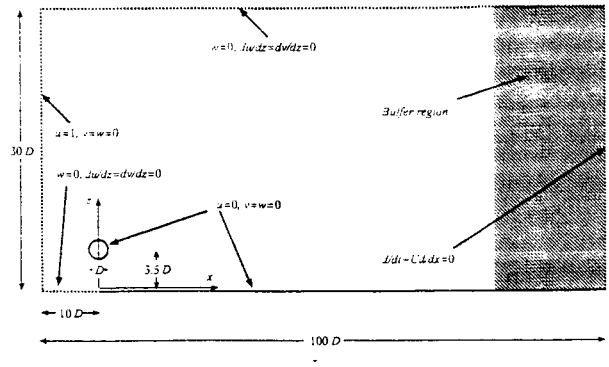

Fig. 2 Sketch of the computational configuration and boundary conditions. The drawing is not to scale.

the boundary layer and of the shear layers emanating from the cylinder. The discretized equations are integrated in time using an explicit fractional time-step method,[7,8] in which all terms are advanced in time using the Adams-Bashforth method. The Poisson equation is then solved using a direct solver, and the velocity is corrected to make the field solenoidal. For the LES, the SGS stresses are parameterized using the Lagrangian Dynamic eddy-viscosity model,[9] which has been shown to give accurate results in transitional flows.

The effect of the cylinder, which does not coincide with the grid lines, is introduced using an "immersed boundary" formulation. In our implementation the enforcement of non-slip boundary conditions on the cylinder surface is performed using a method similar to the the "discrete forcing" approach introduced by Mohd-Yusof[10] and Fadlun *et al.*[11] With this approach, the solution is reconstructed at the grid nodes near the boundary to ensure satisfaction of the no-slip conditions. While Mohd-Yusof[10] and Fadlun *et al.*[11] used a simple one-dimensional reconstruction scheme, in the present study we employ a multidimensional procedure proposed by Balaras,[13] in which the solution is reconstructed along the line normal to the interface.

The code is parallelized using MPI message-passing routines; the parallelization is performed by domain-decomposition process. Except for the Poisson solver, the computational domain is divided into a number subdomains in the z directions, each of which is assigned to one processor. In the Poisson solver, after the velocity divergence is Fourier-transformed in the spanwise directions, each processor is responsible for a set of spanwise modes.

We applied the following boundary conditions (see Fig. 2):

1. At the inlet, a uniform velocity in the x direction was assigned.

2. At the outlet, radiative boundary conditions[17] were given. Furthermore, over the last 30% of the domain (which contains only 5% of the grid points) the mesh was stretched very significantly, to generate a buffer layer in which the equations are effectively parabolized because of the large aspect ratio of the cells.

3. In the spanwise direction, y, periodic conditions were used.

4. In the freestream, we used a slip-wall boundary condition.

5. On the cylinder surface, no-slip conditions were enforced using the methodology described in Balaras.[13] The cylinder was placed at a height of $3.5D$ above the nominal leading-edge of the plate.

6. On the $z = 0$ surface, we used free-slip conditions ($w = 0$, $\partial u/\partial z = \partial v/\partial z = 0$) ahead of the plate, and no-slip conditions ($u_i = 0$) on the plate. A sharp transition between free-slip and no-slip was found to generate numerical oscillations; therefore, a hyperbolic tangent profile was used to merge free-slip and no-slip conditions in a smooth fashion. As a result, the origin of the boundary layer on the plate cannot be determined precisely; in the present calculations, the virtual origin of the boundary layer appears to be approximately $1.5D$ upstream of the actual leading edge.

Two calculations were carried out, corresponding to cases 1 and 2 of Kyriakides *et al.*[4] The geometry for the two cases was the same, but the free-stream velocity was varied to obtain Reynolds numbers Re_D equal to 385 and 1,155, respectively. The definition of the Reynolds number is based on the free-stream velocity and cylinder diameter. The extent of the computational domain in the streamwise and wall-normal directions was $100D$ and $30D$, as shown in Fig. 1. The spanwise width of the domain was $2\pi D$ wide, a length sufficient to include several rib vortices, and to resolve the three-dimensional structures in the cylinder wake.

Code validation

The code used in this paper has been extensively validated for a variety of turbulent[14,15] and re-laminarizing[16] flows. The "immersed boundary" formulation which is used to enforce non-slip boundary conditions on the cylinders surface, has also been extensively tested in the context of the present code.[13] In particular, a series of three-dimensional computations were conducted of the flow around a circular cylinder at $Re_D = 300$. These involved a total number of grid points ranging from 1.5×10^6 to 4.7×10^6. The agreement of the results with reference computations using boundary fitted coordinates demonstrated the accuracy of the method. Details on the above computations can be found in Balaras.[13]

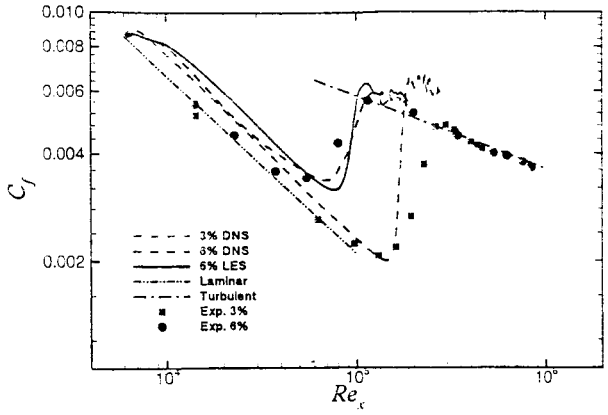

Fig. 3 Streamwise development of the skin-friction coefficient C_f.

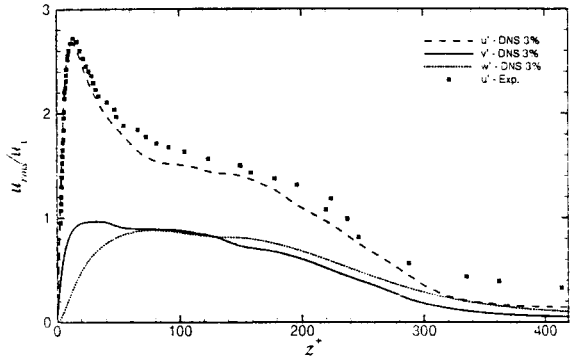

Fig. 4 Profiles of the streamwise turbulence intensity, u_{rms}.

The grid required for accurate simulations of bypass transition needs to be determined carefully. To this end, we performed simulations of bypass transition on a flat plate due to free-stream turbulence. We used the setup adopted by Voke and Yang.[18] The calculation was started at the streamwise location $Re_x \simeq 6,000$; the inflow condition consisted of a Blasius boundary layer, on which turbulent fluctuations were added. The fluctuations were obtained from a separate calculation of spatially developing homogeneous isotropic turbulence. To avoid introducing excessively large fluctuations near the wall, the turbulent fluctuations were windowed in such a way that they vanished at $2\delta_o/3$ (where δ_o is the inflow boundary-layer thickness). Two cases were run, with a 3% and a 6% freestream turbulence amplitude, to match the calculations[18] and the experimental data.[19] The description of the inflow conditions both for the experiment and the LES calculations was not, however, detailed enough to allow us to reproduce exactly the experimental setup.

We performed DNS of both cases. For the 3% case, we $850 \times 96 \times 96$ points to simulate a domain that had dimensions $714\delta_o \times 32\delta_o \times 48\delta_o$; For the 6% case, 550 points were used in the streamwise direction to discretize a box that was $476\delta_o$ long. The mesh was uniform in the spanwise direction, and stretched in the x and z directions. In the transition region, the grid size was approximately $\Delta x = 0.2\delta$, $\Delta y = 0.08\delta$; at least 40 points were used to discretize the local boundary layer thickness, δ. For the LES of the 6% case, $300 \times 64 \times 96$ points were used, resulting in coarser resolution in x and y: $\Delta x = 0.4\delta$, $\Delta y = 0.1\delta$.

The streamwise development of the skin-friction coefficient $C_f = 2\tau_w/\rho U_\infty^2$ is shown in Fig. 3. One can observe a higher skin-friction coefficient in the laminar region, due to the perturbation introduced at the inflow, which generates a pressure disturbance that propagates well inside the boundary layer and distorts the mean-velocity profile in the near-wall region. It was verified that, in the absence of inflow disturbances, the Blasius profile was recovered. The slope of the skin-friction coefficient distribution is, however correct. The transition begins at the correct location for both values of the freestream turbulence intensity, and the extent of the transition region is also predicted with reasonable accuracy. The LES calculation predicts the a slightly delayed beginning of the rise of C_f, and a somewhat more rapid transition; the results are, however, in reasonable agreement with the DNS and the experiments. In Fig. 4 the distributions or the r.m.s. turbulence intensities at $Re_x = 290,000$ (for the 3% freestream turbulence case) are compared with the experimental data of Roach and Brierley.[19] The agreement is again satisfactory, given the uncertainty in the inflow condition generation.

Finally, a grid refinement study was carried out on the real geometry. Two grids were tested, a coarse one that used $576 \times 48 \times 192$ grid points and a medium one with $864 \times 72 \times 288$ points. Calculations on a finer grid with $1056 \times 128 \times 384$ points are currently underway. The coarse grid was similar to the one that gave grid-converged results in the cylinder calculation. Figure 5 shows the mean velocity profile and the trace of the Reynolds stresses $q^2 = \langle u_i' u_i' \rangle$ (throughout this paper $\langle \cdot \rangle$ represents a long-time average, and $f' = f - \langle f \rangle$ is the fluctuating component of f) at three locations downstream of the cylinder. Very little difference can be observed between the coarse and medium grids for the mean velocity profiles; the coarse resolution of the wake and boundary layer results in some difference in q^2 between the coarse and medium meshes, but the agreement is altogether satisfactory. In the following, the medium grid results will be presented.

Notice that the resolution of the boundary layer in the medium grid compares favorably with the bypass transition case mentioned above. In the transition region, the grid spacing was $\Delta x = 0.07\delta$, $\Delta y = 0.06\delta$ (where δ is the local boundary layer thickness). At least 80 points were used to discretize the boundary-layer thickness.

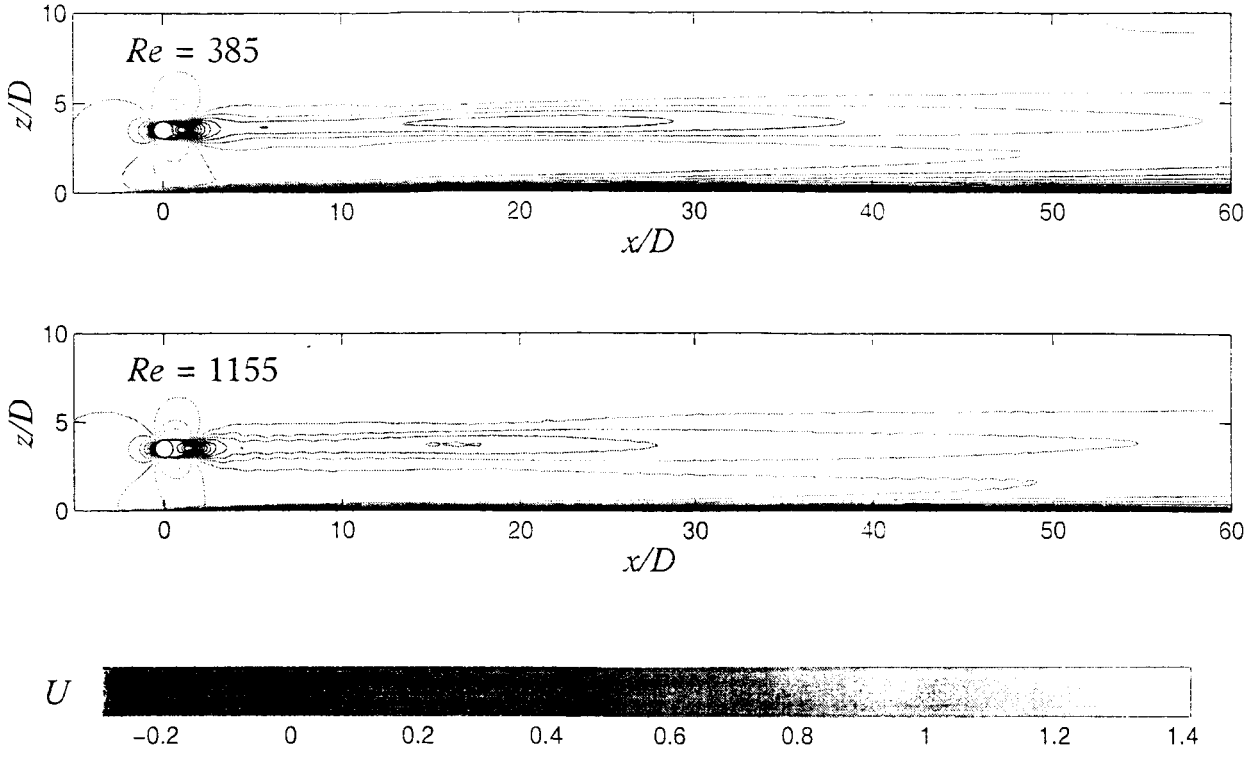

Fig. 6 Mean velocity contours. —— $Re_D = 385$; --- $Re_D = 1,155$.

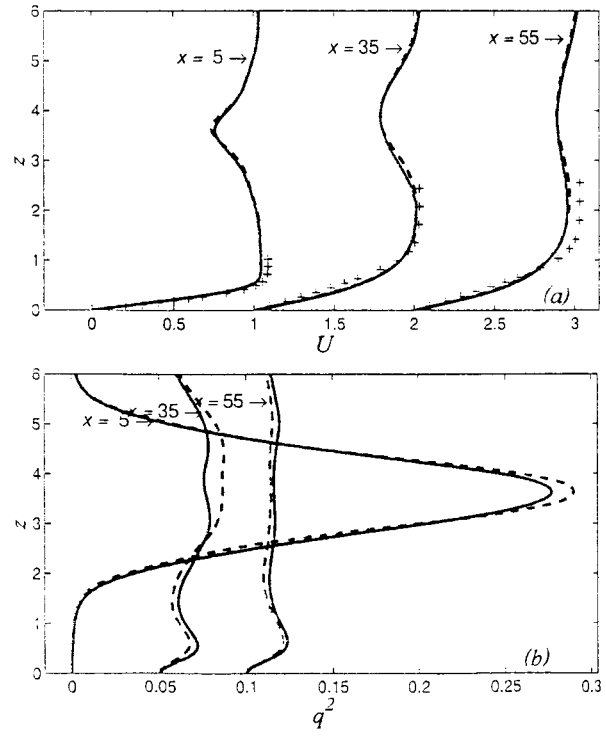

Fig. 5 (a) Mean velocity profiles and (b) profiles of q^2, $Re_D = 385$. —— **$576 \times 48 \times 192$ grid;** --- **$864 \times 72 \times 288$;** × **Blasius solution.**

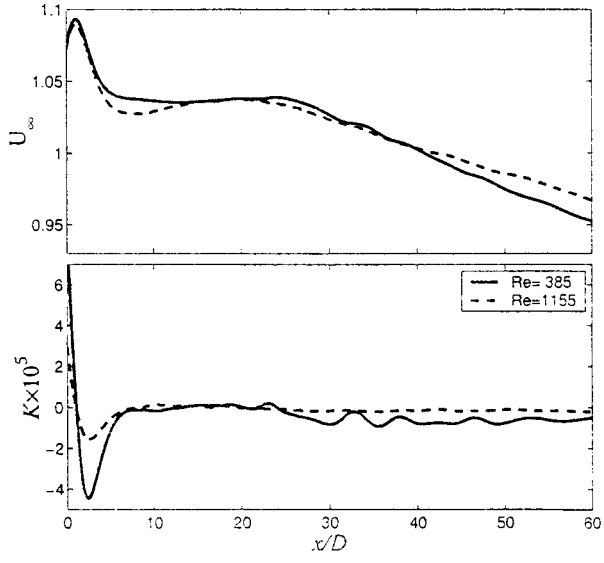

Fig. 7 Streamwise development of: (a) the velocity at the edge of the boundary layer; (b) the acceleration parameter K.

Results and discussion

The mean-velocity contours from the wake/boundary-layer simulations at $Re_D = 385$ and $Re_D = 1,155$ are shown in Fig. 6. As expected, both the wake and the boundary layer are thinner at the higher Reynolds number. No merging is observed within the computational domain. Due to the presence of the cylinder, the boundary layer near

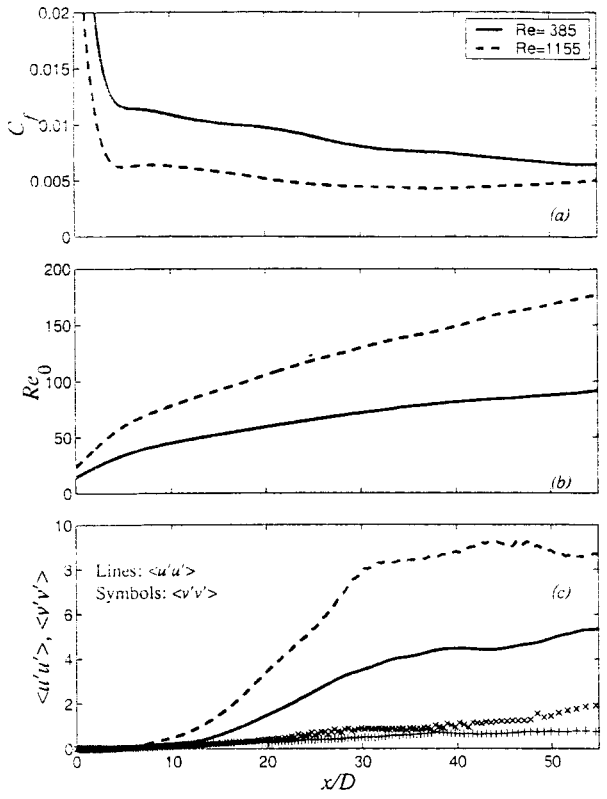

Fig. 8 Streamwise development of statistical quantities. (a) skin friction coefficient C_f; (b) Reynolds number based on the momentum thickness, Re_θ; (c) peak streamwise and spanwise Reynolds stresses in the boundary layer.

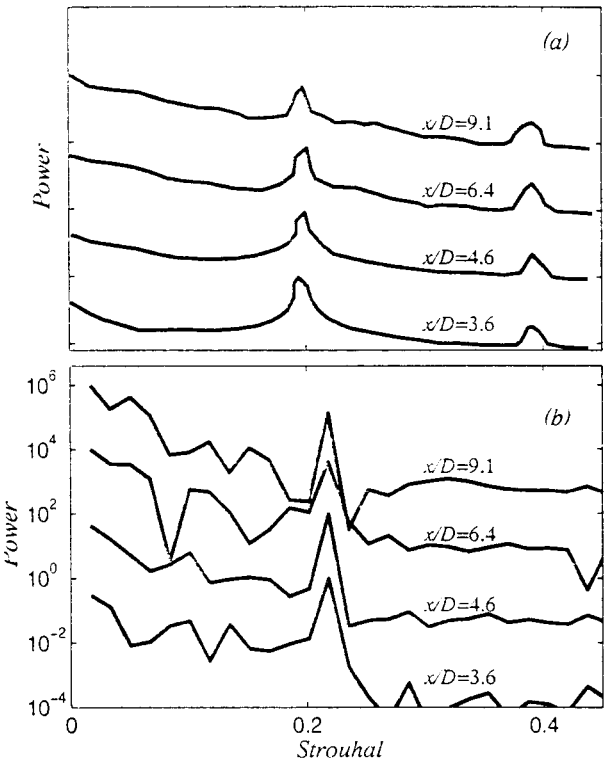

Fig. 9 Power spectra of the streamwise velocity fluctuations near the wall. (a) Data of Kyriakides *et al.*;[4] (b) present calculation, $Re_D = 385$.

the leading edge first encounters an accelerating outer flow, and then a decelerating one. The corresponding acceleration parameter $K = (\nu/U_\infty)(dU_\infty/dx)$ (where U_∞ is the velocity at the edge of the boundary layer) is initially large and positive. The region of large positive values of K is, however, limited to the region $x/D \leq 1$ (Fig. 7); over most of the flat plate the acceleration parameter is below the value that may result in re-laminarization ($K \simeq 3 \times 10^{-6}$). In fact, for $x/D \geq 22$ the boundary layer is subjected to a mild adverse pressure gradient that is expected to favor transition to turbulence.

The streamwise development of several statistical quantities is shown in Fig. 8. The skin friction coefficient C_f (Fig. 8a) from both calculations is very close to the value corresponding to the Blasius boundary layer. In the high Reynolds-number case we observe a significant increase of C_f (towards the end of the computational domain); this issue will be discussed further below. The Reynolds number based on the momentum thickness, Re_θ, is shown in Fig. 8b. For both calculations Re_θ remains very low. As mentioned before, the Re_θ values achieved in the $Re_D = 385$ case are unquestionably below the minimum values at which self-sustained turbulence is typically observed in flat-plate boundary layers. The Re_θ values from the high Reynolds-number calculation towards the end of the computational domain are perhaps marginal in this regard.

The power spectra of the streamwise velocity at $z/D = 0.15$ are compared in Fig. 9 with the experimental data of Kyriakides *et al.*[4] The experimental data was taken from Fig. 7 of the paper cited, which did not specify the distance from the wall at which the data was measured, nor the scale of the ordinate; the frequency has been rescaled to yield a dimensionless Strouhal number. Our calculations are in general agreement with the experimental observations; the shedding frequency is 0.22 (in the experiment a value of 0.21 was observed) and we observe a filling-up of the spectrum at both lower and higher frequencies with distance downstream of the cylinder. We do not observe, however, the harmonic peak measured in the experiment at $St = 0.42$. It is unclear whether this discrepancy is due to experimental or numerical errors, to insufficient sample convergence in the DNS, or to a difference in the location of the measurements.

Kyriakides *et al.*[4] observed that time-traces of the velocity at this height had a sinusoidal behavior up to $x/D \simeq 7.3$ and 2.7 for the low and high Reynolds-number, respectively; they identified transition with the loss of the sinusoidal behavior. The time histories of the velocity fluctuations (not shown) show depar-

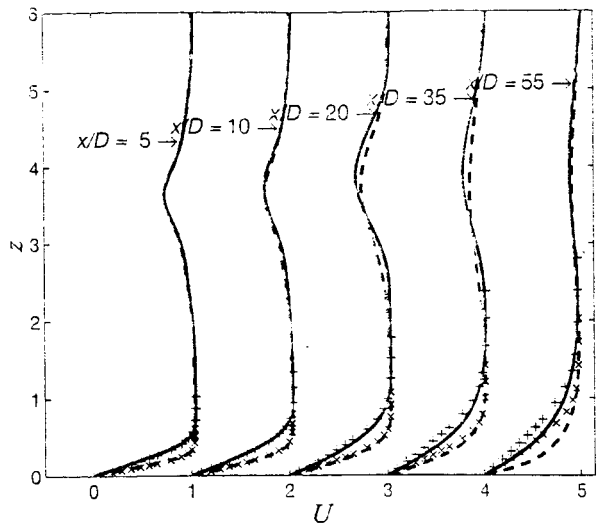

Fig. 10 Mean velocity profiles at various locations. ——— $Re_D = 385$; --- $Re_D = 1,155$; × Blasius profile. Each profile is shifted by 1 unit for clarity.

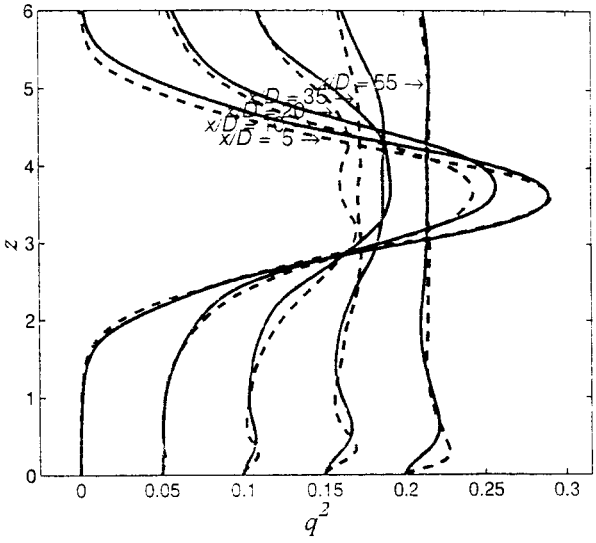

Fig. 11 Profiles of q^2 at various locations. ——— $Re_D = 385$; --- $Re_D = 1,155$. Each profile is shifted by 0.05 units for clarity.

ture from the sinusoidal behavior at similar locations. We believe, however, that a quantitative definition of the onset of transition is more desirable than the subjective one adopted by Kyriakides *et al.*[4] One possibility is to define the location of the transition point in terms of some threshold value of the turbulent fluctuations. Figure 8c shows the developments of the peak $\langle u'u' \rangle$ and $\langle v'v' \rangle$ Reynolds stresses, normalized by the local wall stress τ_w. The streamwise Reynolds stresses reach values comparable to those expected in turbulent flows in the $Re_D = 1,155$ case, while they remain at about half of this level when $Re_D = 385$.

An important measure of transition is the onset of three-dimensionality. We observe that the spanwise Reynolds stress $\langle v'v' \rangle$ begins growing earlier for $Re_D = 385$ than for $Re_D = 1,155$. This is a consequence of the faster spreading of the cylinder wake at the low Reynolds-number. It will be shown later that the first onset of three-dimensionality in the boundary layer is caused by the passage of the vortices shed in the wake of the cylinder. The onset of three-dimensionality in the boundary layer is very well correlated with the onset of three-dimensionality in the wake.

Figures 10 and 11 show the profiles of the mean velocity and q^2 at several locations downstream of the cylinder. We observe a clear separation between the boundary layer and the wake near the leading edge, which disappears as one moves downstream. Up to $x/D = 20$ the velocity profiles agree very well with the Blasius solution at both Reynolds numbers. In the low Reynolds-number case we observe a mild growth of fluctuations in the boundary layer (evidenced both by the streamwise development of $\langle u'u' \rangle$, Fig. 8, and by the profiles of q^2, Fig. 11). These fluctuations, however, appear to be due entirely to the advection caused by the vortices shed by the cylinder, which, as they are

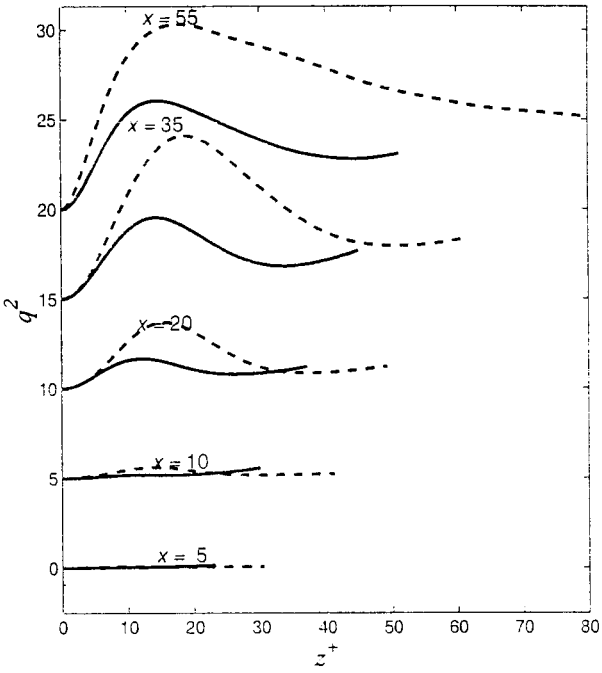

Fig. 12 Profiles of q^2 in wall units at various locations. ——— $Re_D = 385$; --- $Re_D = 1,155$. Each profile is shifted by 5 units for clarity.

convected downstream, induce ejections of low-speed fluid from the near-wall region. These velocity fluctuations, in fact, do not result in the levels of Reynolds shear stress $\langle u'w' \rangle$ typical of the turbulent flat-plate boundary layer (see below).

The high-Reynolds-number calculation shows a different behavior. Significant differences appear in the velocity profile at the downstream locations. At the last location shown ($x/D = 55$), $Re_x \simeq 58,000$ and

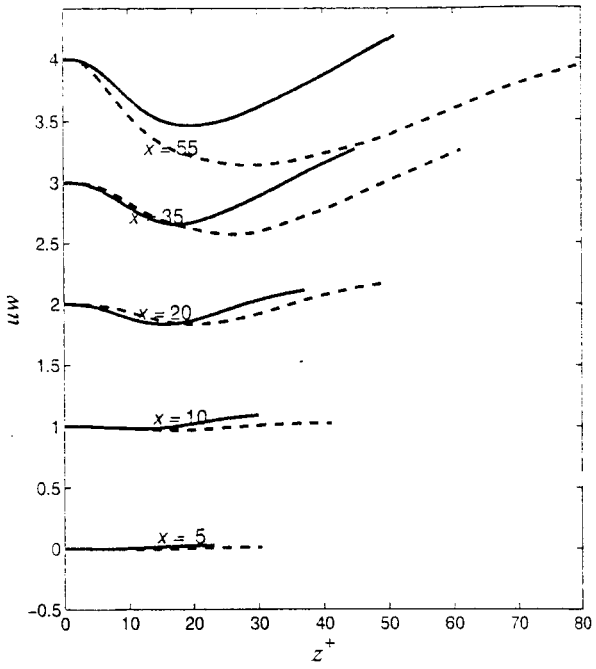

Fig. 13 Profiles of $\langle u'w' \rangle$ in wall units at various locations. ——— $Re_D = 385$; --- $Re_D = 1,155$. Each profile is shifted by 1 unit for clarity.

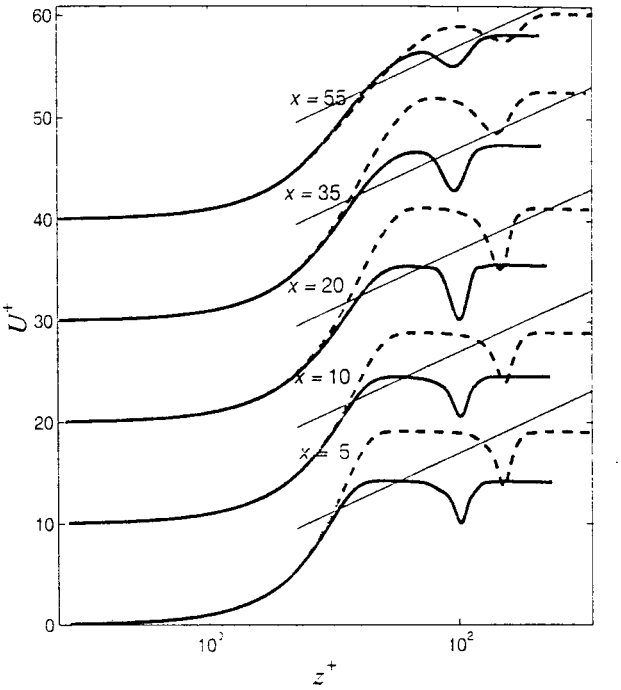

Fig. 14 Mean velocity profiles in wall units at various locations. ——— $Re_D = 385$; --- $Re_D = 1,155$. Each profile is shifted by 10 units for clarity.

$Re_{\delta^*} \simeq 340$. Although the flow has not achieved a fully developed turbulent state yet, there are several indications that transition to turbulence is taking place. The turbulent kinetic energy (Fig. 11), for instance, shows a near-wall peak that is increasing and moving towards the wall. The value of this peak and its location in wall units are those expected in a turbulent flat-plate boundary layer (Fig. 12). The Reynolds shear stress $\langle u'w' \rangle$ (Fig. 13) exhibits a similar behavior: its peak value and distribution for the high-Reynolds-number case are similar to those expected in turbulent flat-plate flows, while in the $Re_D = 385$ case the peak is significantly lower.

The Reynolds stresses appear to move towards a turbulent state more rapidly than the mean velocity profile; the shape factor $H = \delta^*/\theta$ remains close to the laminar value of 2.6 throughout the computational domain, and the mean velocity profile has not achieved a logarithmic profile by the end of the computational domain (Fig. 14). However, significant levels of turbulent fluctuations (r.m.s. levels between 1 and 10% of the freestream velocity) are observed within the boundary layer. At the downstream stations, the freestream turbulence at the edge of the boundary layer is very significant, between 3 and 5% of the velocity at the boundary-layer edge (for the low and high-Reynolds number cases, respectively), levels that are able to trigger bypass transition in boundary layers. Computations that use a longer domain should be carried out to determine the exact route to turbulence in the present configuration.

Figures 15 and 16 show instantaneous contours of the streamwise velocity fluctuations, and iso-surfaces of the second invariant of the velocity gradient tensor,

$$Q = -\frac{1}{2}\frac{\partial u_i}{\partial x_j}\frac{\partial u_j}{\partial x_i} = -\frac{1}{2}\left(S_{ij}S_{ij} - \Omega_{ij}\Omega_{ij}\right), \quad (5)$$

where S_{ij} is the strain-rate and Ω_{ij} the rotation-rate tensor. In regions where $Q > 0$, the vorticity is due to rotational motions, rather than to shear.

In the low-Reynolds-number case (Fig. 15) the cylinder wake is very well-defined; staggered rows of quasi-2D vortices are shed, which are joined by clearly observable rib vortices. Three-dimensionalities quickly develop. There is a high correlation between the appearance of three-dimensionalities in the rollers, and the appearance of low- and high-speed streaks in the boundary layer (a very clear example can be observed around $x/D = 20$). This feature is connected to the increase of the spanwise Reynolds stress $\langle v'v' \rangle$ mentioned above. These streaks are convected with the freestream velocity, confirming the observation that they are induced by the outer flow: in turbulent flows, the typical near-wall streaks, which are generated in the inner layer, are convected at speeds that are 60–70% of the freestream velocity.

Another effect of the shed vortices on the near-wall region can be observed in Fig. 15c. Corresponding to the vortex street, one can observe alternating regions of high- and low-speed fluctuations, due to the advection from the upper and lower rows of vortices, respectively. These regions correspond to Q2 and Q4

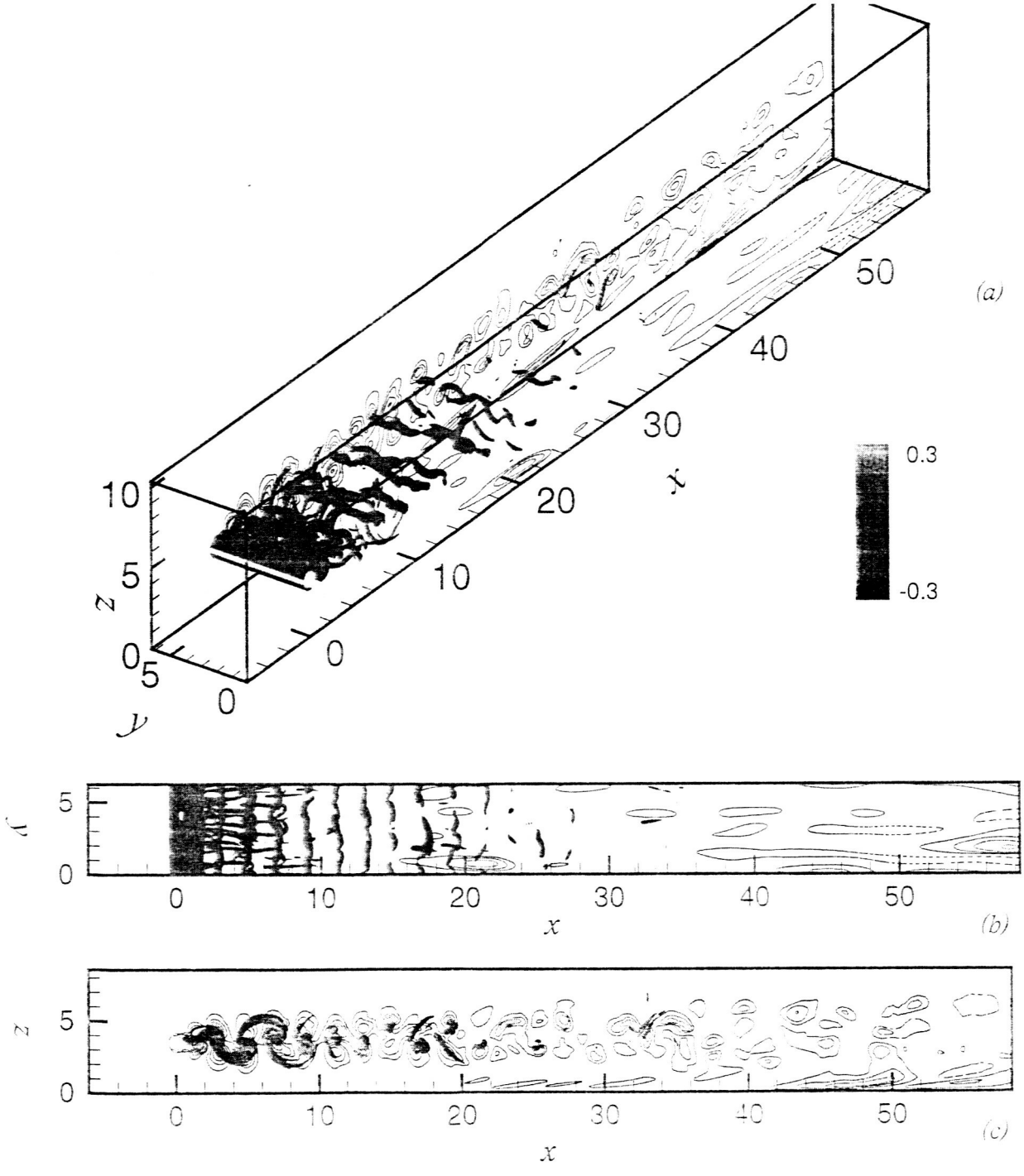

Fig. 15 Isosurfaces of Q, and contours of the streamwise velocity fluctuations in a $xz-$plane and in the $z/D = 0.2$ plane. $Re_D = 385$. (a) Prospective view; (b) top view; (c) side view.

events,[20] and are responsible for regions of significant correlation $u'w'$. As the rollers become weaker, no new streaks are generated, and the flow does not appear to evolve into a fully turbulent state, the main disturbances being due to the streaks that are convected downstream, and weaken progressively.

At the high Reynolds-number (Fig. 16) a somewhat different picture emerges. Smaller-scale vortices can be observed in the wake, consistent with the increased Reynolds number. Also, the wake breaks down more rapidly. Well-defined rollers and rib vortices can, nonetheless, be observed. Some low-speed regions in the boundary layer can still be observed, corresponding to the onset of three-dimensionality in the rollers; unlike the low-Reynolds-number case, however, these streaks do not weaken significantly as they are convected downstream. The decreased viscous dissipation due to the increased Reynolds number certainly plays a role in this, but a self-sustaining turbulence generation cycle may also be beginning to appear. This conjecture is supported by the appearance of quasi-streamwise vortices in the near-wall region for $x/D > 50$.

Conclusions

The work presented in this paper had a two-fold objective, namely, to establish the accuracy of the numerical code for wake-boundary-layer interaction problems and to clarify unanswered questions regarding prior experiments[4] related to such interactions. We believe that both of these goals have been nearly met through the work described here. In addition to code validation for building-block problems involving the isolated problems of cylinder wake and bypass transition in a flat-plate boundary layer, we have carried out large-eddy and direct simulations to understand the details of the strong interaction between a cylinder wake and a flat-plate boundary layer at two Reynolds numbers ($Re_D = 385$ and 1,155) selected from the low-Re_D range in the experiment, for which transition was apparently observed.

We observe a region in which the cylinder wake perturbs the boundary layer by advecting low-speed fluid from the wall into the outer region, and high-speed fluid from the core towards the wall, as rollers of alternating rotation are convected above the boundary layer. Three-dimensional disturbances appear in the boundary layer in correspondence to kinks in the spanwise rollers. The appearance of streamwise vorticity in the wake is visually well-correlated with the presence of low- and high-speed streaks near the wall. This, and the fact that these streaks are convected downstream at the freestream velocity (rather than a convection velocity typical of near-wall phenomena) indicate that the perturbations in the boundary layer are forced from the outside, and not generated within the boundary layer itself. As the wake decays, the advection effect becomes less significant, but the wake generates high levels of freestream turbulence, that are expected to affect the flow downstream. In the low-Reynolds-number case the flow tends towards a more quiescent state towards the end of the computational domain and the statistics never reach turbulent levels. In the high-Reynolds-number case, on the other hand, the appearance of coherent, quasi-streamwise vortices is observed, which might be the prelude to the establishment of a self-generating cycle of sweeps and ejections. This was supported by the establishmnent of Reynolds-stress levels comparable to those observed in turbulent flows.

While some features of the computed flow fields are in satisfactory agreement with the measured data, the simulations indicate that transition does not really take place at the lower Reynolds number: the boundary layer is simply buffeted by the unsteady Kármán vortex street shed by the cylinder. For $Re_D = 385$ the fluctuations generated in this manner cannot be self-sustained due to low-Reynolds-number effects, and the boundary-layer flow does not transition to turbulence. We believe that the cause behind the discrepancy between the observations of Kyriakides *et al.*[4] and the above results is to be found in an unsatisfactory criterion for transition detection in the experiment, and in the lack of sufficiently detailed measurements of the type particularly required for transition studies. In contrast, in the higher Reynolds-number case, boundary-layer fluctuations persist even after the wake has decayed. This can be attributed, in part, to the spatial growth of the boundary layer during the interaction, which brings the Re_θ values closer to the typical range of minimum critical Reynolds numbers required for self-sustained turbulence in zero-pressure-gradient flows; some evidence could be observed that a self-sustaining turbulence generation cycle was beginning to be established.

Near-term extensions to this work will involve additional simulations to clarify the flow behavior downstream of the present domain. We also plan to investigate the possibility of higher-Re simulations, which will also allow the present study of strong wake interactions to be extended to weak interactions. It will be interesting to find out the extent of similarities between the weak interactions and the familiar case of bypass transition due to moderate levels of free-stream turbulence.

Acknowledgments

The first, third and fourth authors acknowledge the financial support of the NASA Langley Research Center, under Grant NAG12285.

References

[1]Meredith, P. 1993 *AGARD CP-515*, 19.1.

[2]Squire L. C. 1989 *Prog. Aerospace Sci.* **26**, 261–288.

[3]Zhou, M.D., and Squire, L.C. 1985 *J. Aeronaut.* **89**, 72.

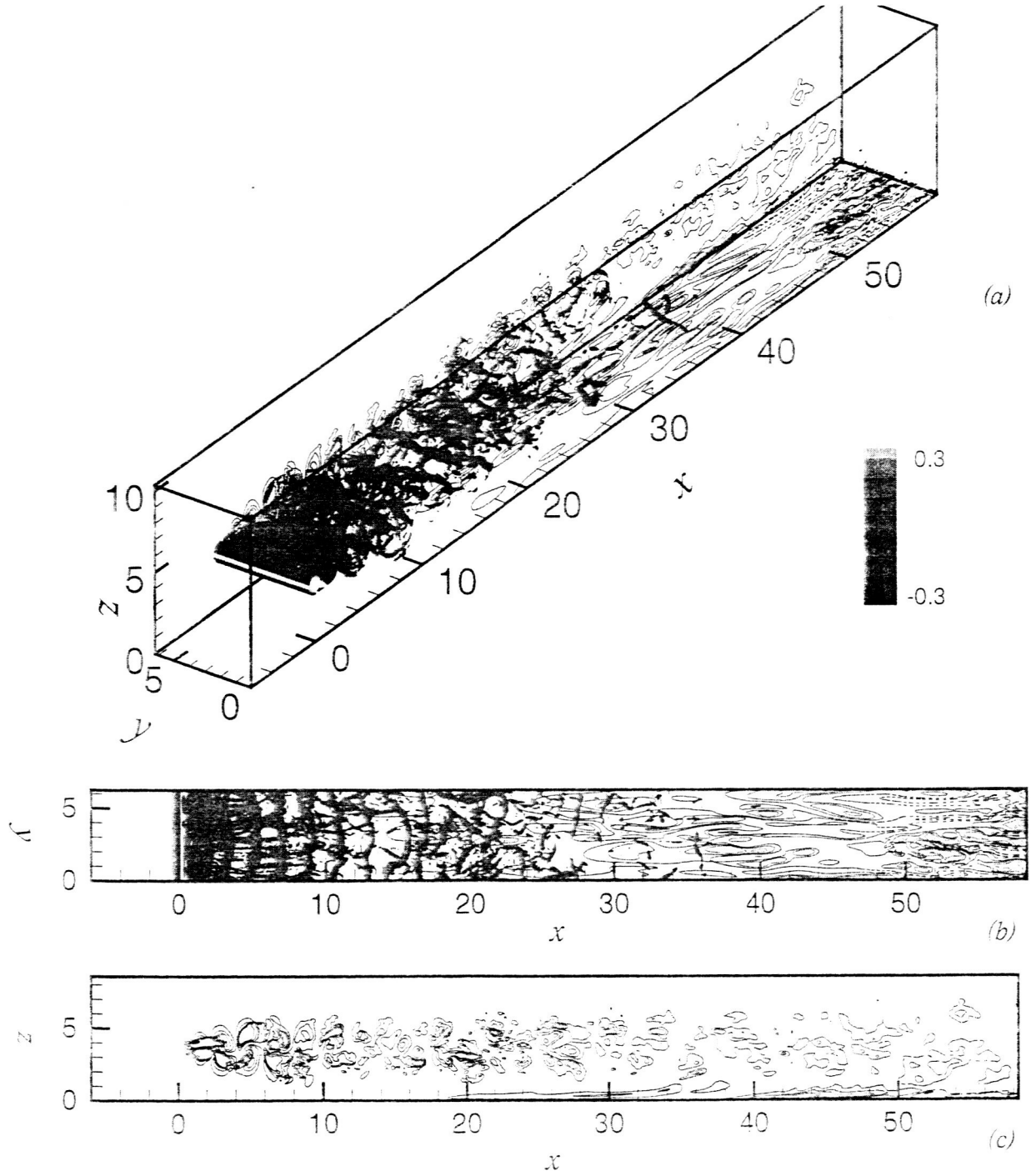

Fig. 16 **Isosurfaces of Q, and contours of the streamwise velocity fluctuations in a $xz-$plane and in the $z/D = 0.2$ plane.** $Re_D = 1,155$.

[4]Kyriakides N.K., Kastrinakis, E.G., Nychas, S.G., Goulas, A. 1996 *Proc. Inst. Mech. Eng.* **210**, 167.
[5]Kyriakides N.K., Kastrinakis, E.G., Nychas, S.G., Goulas, A. 1999 *AIAA J* **37**, 1197.
[6]Kyriakides N.K., Kastrinakis, E.G., Nychas, S.G., Goulas, A. 1999 *Eur J. Mech. B-Fluid* **18**, 1049.
[7]Chorin, A. J. 1968 *Math. Comput.* **22**, 745.
[8]Kim, J. and Moin, P. 1985 *J. Comput. Phys.* **59** 308.
[9]Meneveau, C., Lund, T. S., and Cabot, W. H. 1996 *J. Fluid Mech.* **319** 353–385.
[10]Mohd-Yusof, J. 1997 in *CTR Annu. Res. Briefs 1997*, NASA Ames/Stanford University, 317.
[11]Fadlun, E.A., Verzicco, R., Orlandi, P., Mohd-Yusof, J. 2000 *J. Comput. Phys.* **161** 35.
[12]Verzicco, R., Mohd-Yusof, J., Orlandi, P., Haworth, D. 2000 *AIAA J.* 38 427.
[13]Balaras, E. 2002 Submitted to *Comput. and Fluids.*
[14]Balaras, E., Benocci, C., and Piomelli, U. 1995 *Theoret. Comput. Fluid Dyn.* **7** 207.
[15]Balaras, E., Piomelli, U., and Wallace, J.M. 2001 *J. Fluid Mech.*, **446**, 1.
[16]Piomelli, U., Balaras, E., & Pascarelli, A. 2000 *J. Turbulence* **1**, 001.
[17]Orlanski, I. 1976 *J. Comput. Phys.* **21**, 251.
[18]Voke, P., and Yang, Z. 1995 *Phys. Fluids* **7**, 2256.
[19]Roach, P.E., and Brierley, D.H. 1992 In *Numerical Simulation of unsteady flows and transition to turbulence*, O. Pironneau, W. Rodi, I.L. Rhyming, A.M. Savill and T.V. Truong, eds. Cambridge, 318.
[20]Wallace, J.M., Brodkey, R.S., and Eckelman, H 1972 *J. Fluid Mech.* **54**, 39.